Research Square

Preprints are preliminary reports that have not undergone peer review.
They should not be considered conclusive, used to inform clinical practice,
or referenced by the media as validated information.

Peak Proton Flux of Solar Energetic Particle Events from Soft X-Ray Flares: The Garcia–Balch Relations Compared with Quantum Regression

Igor Davydenkov

davydenkov.ii@phystech.edu

Space Research Institute

Research Article

Keywords:

Posted Date: November 18th, 2026

DOI: https://doi.org/10.21203/rs.3.rs-11652000/v1

License: This work is licensed under a Creative Commons Attribution 4.0 International License.
Read Full License

Additional Declarations: No competing interests reported.

Peak Proton Flux of Solar Energetic Particle Events from Soft X-Ray Flares: The Garcia–Balch Relations Compared with Quantum Regression

Igor Davydenkov

Space Research Institute of the Russian Academy of Sciences, Profsoyuznaya Street 84/32, Moscow 117997, Russia

Corresponding author: Igor Davydenkov, davydenkov.ii@phystech.edu

Abstract

We extend the peak-flux relations of Balch (2008) and Garcia (2004a), last verified on solar cycle 23, to 111 events of cycles 23–25 (1997–2026), and compare them with variational quantum regression (VQR). With published coefficients the Balch relation keeps its original skill on these independent data, including the first GOES-R cycle (correlation 0.49, root-mean-square error 0.83 dex). The peak flux depends on the flare fluence in a curved way: the local exponent is 0.85 at $0.1\,\mathrm{J\,m^{-2}}$, close to the published 0.82, and steepens for the largest flares. Emission measure and temperature add no information beyond the integrated emission. The scatter is organized by the time of the proton maximum. Events peaking within 12 hours lie near the nominal connection (median W58) and follow the fluence law, whereas those peaking after a day lie near central meridian (median W11) and are underestimated by 0.4–0.7 dex, as expected if their maximum is set near shock passage. VQR matches the best classical models. With only fluence and connection it reaches a mean absolute error of 0.567 dex, against 0.705 dex for climatology and 0.636 dex for the published law, a difference from the latter that is within the uncertainties. It captures the curvature of the law without an assumed form and with a small generalization gap. Compact classical models do equally well, a small neural network (0.550 dex) and a ridge regression on four Fourier features (0.542 dex), and entanglement brings no gain, so no benefit specific to quantum effects is found. Adding the proton flux observed 3–6 hours after onset lowers the error of events still rising from about 0.6 to 0.4 dex, so the accuracy at the flare end is limited by missing information on the shock at 1 AU rather than by the model.

Keywords: Energetic Particles, Protons; Flares, Forecasting; Coronal Mass Ejections; X-Ray Bursts, Spectrum; Solar Cycle, Observations

1. Introduction

Large solar energetic particle (SEP) events are the main short-term radiation hazard for crews and spacecraft outside the Earth's magnetosphere (Reames, 1999; Desai and Giacalone, 2016;

Papaioannou et al., 2025). Their size at the Earth is shaped by three stages: the release of energy in the flare and eruption, the acceleration of protons at the coronal and interplanetary shock, and the transport of those protons along the interplanetary magnetic field. Forecasters must nevertheless estimate the size within minutes of the flare, when only the first of these stages has been observed.

For this reason the soft X-ray flare measured by the *Geostationary Operational Environmental Satellites* (GOES) has been the classical predictor. Two relations from the National Oceanic and Atmospheric Administration (NOAA) express the idea explicitly. Balch (1999, 2008) gave the power law used in the PROTONS model of the Space Weather Prediction Center (SWPC), in which the peak flux above 10 MeV follows the time-integrated 1–8 Å flux of the flare. Garcia (2004a) gave a relation in terms of the flare emission measure, peak X-ray flux, and duration, based on his derivation of temperature and emission measure from the two GOES channels (Garcia, 1994a, 1994b). We call them together the Garcia–Balch relations, while keeping the two equations separate.

The physical basis of such relations deserves attention. Large gradual proton events are mainly attributed to CME-driven shocks (Reames, 1999, 2013; Cliver, Kahler, and Reames, 2004; Desai and Giacalone, 2016), so a correlation with flare emission may largely reflect the big-flare syndrome of Kahler (1982): energetic eruptions produce both strong flares and fast CMEs. A direct flare contribution remains possible (Trottet et al., 2015; Dierckxsens et al., 2015). Empirically the link is persistent. Flare X-ray properties organize proton events over three solar cycles (Belov et al., 2005; Belov, 2009), and Papaioannou et al. (2023) recently derived a scaling of the peak proton flux with the flare peak X-ray flux for well-connected events.

The published verification of the peak-flux relations ends with cycle 23. To the best of our knowledge, Balch (2008) is the last publication that states the formula and verifies it, on 127 events from 1986–2004, with a correlation coefficient of 0.524 and a standard error of 0.870 in the logarithm. Whitman et al. (2023) list PROTONS as an operational model, Bain et al. (2021) evaluate the SWPC forecast products over cycles 23 and 24 rather than the peak-flux relation, and Papaioannou et al. (2025) describe the approach among the early nowcasting systems. The temperature line of Garcia's work has continued in occurrence forecasting and in studies of flare–CME relations (Kahler and Ling, 2018, 2020, 2022, 2023; Struminsky, Sadovskii, and Grigorieva, 2024). Cycle 24 and cycle 25, the first measured with the GOES-R series and with a changed operational flux scale (Janssens et al., 2025), have thus remained outside the record of these relations.

Forecast research has meanwhile moved towards multi-input statistical and machine-learning models (Kahler, Cliver, and Ling, 2007; Laurenza et al., 2009; Núñez, 2011; Alberti et al., 2017; Anastasiadis et al., 2017; Swalwell, Dalla, and Walsh, 2017; Lavasa et al., 2021; Kasapis et al., 2022; Papaioannou et al., 2022; Ali et al., 2024, 2025; Hosseinzadeh, Filali Boubrahimi, and

Hamdi, 2024; Rotti, Aydin, and Martens, 2024; Yu et al., 2026). Variational quantum circuits are a recent addition to this family. They represent a smooth non-linear function with a modest number of parameters, which is attractive for the small samples typical of proton events. We apply variational quantum regression (VQR) with data re-uploading (Pérez-Salinas et al., 2020) to the peak flux, and we use it in two ways: as a forecast model, and as a probe of the shape of the flare–proton relation that does not presuppose a functional form.

Our aims are to (i) extend the Balch and Garcia relations to 111 events of cycles 23–25 with the published coefficients, (ii) determine how the peak flux scales with the flare fluence and what organizes the scatter around that scaling, and (iii) assess what quantum regression adds to the classical relations.

2. The Garcia–Balch Relations

2.1. BALCH (2008)

The predicted maximum flux above 10 MeV, in proton flux units (1 pfu = 1 particle $\mathrm{cm^{-2}\,s^{-1}\,sr^{-1}}$), is

$$\Phi_{\mathrm{B}} = 10\,\alpha \left(\frac{X_{\mathrm{int}}}{0.00987} \right)^{0.82}, \tag{1}$$

where X_{int} is the 1–8 Å flux in $\mathrm{J\,m^{-2}}$ integrated from the onset of the X-ray event to its half-power point, the time after maximum when the flux has fallen halfway from the maximum to the pre-event background. The factor α uses the integrated flux X_{pf} of the most recent previous event in the same active region,

$$\alpha = \left(\frac{X_{\mathrm{pf}}}{0.167} \right)^{1.146} \text{ if } X_{\mathrm{pf}} > 0.08, \qquad \alpha = 1 \text{ otherwise.} \tag{2}$$

The coefficients come from events of 1976–1995 (Balch, 1999). None of our events falls in that period, so applied to our sample Equations (1) and (2) are a genuinely independent forecast with no free parameter.

2.2. GARCIA (2004A)

Garcia (2004a) found that among the parameters he examined the emission measure correlates best with the proton magnitude and the temperature worst. His least-squares combination is

$$\log_{10} \Phi_{\mathrm{G}} = -115.67 + 2.34\,\mathrm{EM} - 1055\,X + 0.44\,\Delta t, \tag{3}$$

where EM is the logarithm of the emission measure in $\mathrm{cm^{-3}}$, X the peak 1–8 Å flux in $\mathrm{W\,m^{-2}}$, and Δt the time in hours from flare onset until the 0.5–4 Å flux falls to 25 % of its peak. Garcia quoted a dispersion of 0.54 in the logarithm for flares of lower than average temperature; he

excluded hotter flares from the fit. A companion paper (Garcia, 2004b) extended the approach to hard X-rays, which we do not use because no homogeneous series exists for the whole period. Equation (3) depends strongly on the absolute calibration of EM, which matters below.

3. Data

3.1. PROTON EVENTS

The sample starts from the NOAA list of proton events with a peak above 10 pfu at >10 MeV and keeps the events from August 1996 onward with a NOAA-attributed flare that has a matching entry in the Heliophysics Event Knowledgebase (Hurlburt et al., 2012), a known heliographic location, an onset after the flare peak, and a delay of no more than 24 hours from the flare peak to the NOAA begin time. Re-crossings of the threshold are removed. This gives 112 events, with 61, 25, and 26 events in cycles 23, 24, and 25, from 4 November 1997 to 18 January 2026. The target is $y = \log_{10}$ of the NOAA peak flux. One event (17 June 2003, M6.8) falls in a gap of the 1-minute GOES records we hold, so all scores below refer to 111 events.

The NOAA peak is the maximum of the whole event at geostationary orbit. It may therefore be reached at the passage of an interplanetary shock, as an energetic storm particle (ESP) increase, many hours or days after the flare. Balch (2008) treated events that reached threshold only through an ESP increase, and events from behind the limb, as a priori misses. We keep them: a forecaster at the time of the flare cannot exclude them. Subsets are reported in Section 5..

3.2. X-RAY MEASUREMENTS

From the 1-minute GOES XRS records we measure, for each flare, the peak 1–8 Å flux, the background (the 10th percentile of the 30 minutes before onset), $X_{\rm int}$, and Δt. The onset and end times are those of the flare list. The half-power point follows the definition of Balch (2008); it is not allowed to pass the catalogued end time, which uses the same definition, because the integral would otherwise run into a later flare in the same active region. The entry for the X2.3 flare of 6 June 2000 was a fragment 10 minutes after the true maximum, and we replaced it by the times of the GOES light curve (14:58, 15:25, and 15:40 UT).

The flux scale requires care. From GOES-8 until 2019 the operational fluxes were scaled down, and when SWPC moved to GOES-16 in December 2019 it stopped applying this factor (Janssens et al., 2025). Equations (1) and (3) were calibrated on the older scale. We therefore put every event on the operational scale by multiplying reprocessed and GOES-R fluxes by the SWPC factors, 0.70 in the 1–8 Å channel and 0.85 in the 0.5–4 Å channel. The records we hold mix both scales, so the choice for each event before 2020 is made by comparing the

measured peak with the catalogued class. The saturated flares of October and November 2003 are handled separately: the measured peak of the reprocessed series, rescaled, stands in for the clipped operational value.

The temperature and emission measure come from the background-subtracted fluxes at the 1–8 Å maximum with the isothermal expressions of Thomas, Starr, and Crannell (1985). Garcia (1994a) derived his own calibration and later authors have updated the response functions (White, Thomas, and Schwartz, 2005; Ryan et al., 2012), so this reproduction of EM in Equation (3) is only approximate. White and Desnoes (2026) show that the GOES emission measures themselves can be low by up to 50 % relative to extreme-ultraviolet values.

For α we take the most recent earlier flare of class C1 or above with the same NOAA active-region number within 14 days, using the flare catalogue of the Heliophysics Event Knowledge-base with NOAA region numbers. Only 3 of the 111 events have $X_{\rm pf} > 0.08\,\mathrm{J\,m^{-2}}$, so α has little effect in this sample; 31 events have no earlier flare with a matching region number and take $\alpha = 1$.

4. Forecast Models

4.1. PUBLISHED AND REFITTED RELATIONS

We use Equations (1)–(3) exactly as published. Because a fixed offset in a calibration can dominate a score, we also refit the same functional forms by least squares: the fluence law $y = a + b \log_{10} X_{\rm int}$, the same law with a Gaussian factor $\exp[-(\lambda - 52.5^\circ)^2/2(12^\circ)^2]$ of the flare longitude λ, which peaks at the nominal footpoint of the Parker spiral, and the Garcia form in EM, X, and Δt. The reference without flare information is climatology, the median of the training events.

4.2. QUANTUM REGRESSION

VQR is a regression model built on a parameterized quantum circuit. Each observable is assigned to one qubit and enters as a rotation angle after a quantile mapping, which makes the model insensitive to the very wide range of the inputs. The circuit has three layers. In each layer all inputs are encoded again, followed by trainable rotations and, for pairs of qubits chosen in advance from physical links such as connection and CME speed, by controlled rotations that entangle them. Because an input is encoded repeatedly, the output is a smooth, truncated Fourier-type function of that input (Pérez-Salinas et al., 2020; Schuld, Sweke, and Meyer, 2021), and no form of the law has to be assumed. The expectation values $\langle Z_j \rangle$ of the final state are mapped to y by a ridge regression.

The circuit parameters are trained against a smoothed target from a linear and a shallow

boosted model of the training events, and the forecast averages three random initializations. All circuits are simulated exactly and without noise on a classical computer, so this study concerns the model class and not quantum hardware. The settings were fixed in advance and not tuned for the peak flux.

The full model has twelve inputs: the Parker connection factor $\cos(\lambda - \lambda_{\mathrm{P}})$, the flare peak flux, X_{int}, rise time, and duration, and a flag for a preceding proton event within 72 hours (six flare inputs); the CME speed and width and the rise of 175–315 keV electrons in the *Electron, Proton, and Alpha Monitor* (Gold et al., 1998); and three measures of the direction of the interplanetary magnetic field in the 6 hours before the flare from the OMNI data (King and Papitashvili, 2005). A CME from the catalogue of Yashiro et al. (2004; see also Gopalswamy et al., 2009) is used only if its first reference time is within 60 minutes of the flare peak. We also train the circuit on the inputs of the X-ray relations alone: fluence and connection (two qubits) and EM, peak flux, and Δt (three qubits). In the two-qubit case no pair is coupled, so that circuit contains no entanglement. Random forests (Breiman, 2001) and ridge regressions on each input set serve as classical references.

4.3. EVALUATION

Events of one year often come from the same active region, so each year is forecast by models trained on all other years. In addition, models are trained on the events before 2020 and applied to cycle 25. Forecasts are conditional on the occurrence of a proton event, as in the peak-flux verification of Balch (2008). The VQR forecast is issued at the flare end, a median of 18 minutes after the flare peak, 2.6 hours before the NOAA begin time, and 11.8 hours before the proton maximum. The half-power point comes at 18 minutes and the end of Δt at 25 minutes after the peak, so all forecasts are available at nearly the same time.

We quote the mean absolute error (MAE) of y in dex. An MAE of 0.6 dex is a typical error of a factor of 4 in the flux. Tables also give the mean error (bias), the root-mean-square error (RMSE), the median multiplicative error, and the correlation of the logarithms. Model differences are paired by event, with 95 % bootstrap intervals (Efron and Tibshirani, 1993) and Wilcoxon (1945) signed-rank probabilities.

5. Results

5.1. HOW THE PEAK FLUX SCALES WITH THE FLARE FLUENCE

Figure 1 shows the peak flux against X_{int}. For scale, a value of $0.1\,\mathrm{J\,m^{-2}}$, near the sample median, corresponds to about 3×10^{29} erg radiated in the 1–8 Å band up to the half-power point, a small part of the energy of a large eruption (Emslie et al., 2012). The peak flux rises

with this energy over nearly four decades of fluence, with a scatter of about a factor of 5 at fixed fluence.

The Balch relation carries over well to the new data. With the published coefficients and no adjustment it gives a correlation of 0.49 and an RMSE of 0.83 dex (Table 1), close to the 0.524 and 0.870 of Balch (2008). These events lie entirely outside its calibration period, up to 30 years later, and include a new instrument generation. The relation is low on average by -0.38 dex, and its typical multiplicative error is 2.9. The result is not sensitive to the details of the measurement: background subtraction, the triangular proxy for the fluence, or removal of events behind the limb change the MAE by less than 0.03 dex. Using the true irradiance scale with the published coefficients reduces the bias to -0.24 dex.

A power law fitted to these events has an exponent of 0.71 [0.45, 1.05], consistent with the published 0.82. A sublinear exponent, however, needs care, because the sample is selected above 10 pfu and this removes weak events at low fluence. A fit that allows for this truncation gives 1.33 [0.81, 1.94]. The data therefore permit a proportional or steeper dependence of the peak flux on the radiated energy.

The relation is in fact curved. The residuals of the refitted power law in the five quintiles of $X_{\rm int}$ are $+0.14$, -0.27, -0.24, $+0.10$, and $+0.30$ dex. A parabola,

$$y = a + b \log_{10} X_{\rm int} + c \, (\log_{10} X_{\rm int})^2, \tag{4}$$

with $a = 3.34$, $b = 1.76$ [1.17, 2.47], and $c = 0.45$ [0.22, 0.69], reduces the out-of-sample MAE to 0.556 dex and raises the correlation to 0.58. The local exponent $b + 2c \log_{10} X_{\rm int}$ is 0.85 at 0.1 J m^{-2}, in agreement with the value of Balch (2008) for a typical event, and it rises to 1.76 at 1 J m^{-2}. The largest flares are thus followed by more than proportionally large proton events. The two ends of the curve have different meanings. The steepening at high fluence is a property of the events and is examined in Section 5.3.. The upturn below about 0.011 J m^{-2} is a selection effect: with a floor of 10 pfu, an event from a weak flare enters the sample only if its protons are much stronger than the flare suggests. The seven such events are flares of class C1.2 to M1.2, one of them (14 November 1998, 314 pfu) behind the west limb, where the X-ray emission is partly hidden. Equation (4) therefore describes events that do occur. It was chosen after inspection of the residuals and should be confirmed on future events.

5.2. TEMPERATURE AND EMISSION MEASURE

Garcia (2004a) found that the emission measure is the flare quantity most closely related to the proton magnitude and the temperature the least. Our data agree: Equation (3) reproduces the ordering of the events, with a correlation of 0.45. Its absolute level, however, depends strongly on the emission-measure scale, since the coefficient of EM is 2.34. With our emission measures the forecasts are low by -1.04 dex, and a shift of only 0.38 dex in EM, within the known

differences among GOES calibrations (Garcia, 1994a; White, Thomas, and Schwartz, 2005; White and Desnoes, 2026), accounts for this. Refitted with its own variables the Garcia form performs as well as the fluence law (MAE 0.612 against 0.603 dex). Plasma diagnostics add no information on the peak flux beyond the integrated emission, which is consistent with the view that both measure the overall scale of the energy release.

5.3. THE TIME OF THE PROTON MAXIMUM AND THE ROLE OF THE SHOCK

The scatter around the fluence law has a clear physical organization (Table 2, Figure 2). We divide the events by the time from the flare maximum to the NOAA proton maximum. This time is not known when a forecast is issued, so the division is a diagnostic and not a forecast.

Events that peak within 12 hours come from the western hemisphere, with a median longitude of W58, close to the nominal magnetic connection, and only 7 % come from the east. For these 56 events the Balch relation works well: the MAE is 0.46 dex and the bias -0.16 dex. Events that peak later than 24 hours have a median longitude of W11, near central meridian, and 34 % come from the east. Their median peak flux is 364 pfu against 61 pfu, and they include 9 of the 18 events above 1000 pfu. For them all forecasts are low, by -0.72 dex for the Balch relation and -0.36 dex for VQR. The time of maximum correlates with longitude (ρ =-0.34, $p = 0.0002$).

This is the classical pattern of gradual events (Cane, Reames, and von Rosenvinge, 1988; Reames, 1999). For a well-connected western source the observer's field line reaches the shock near the Sun, and the maximum comes early, while the particles are released from the strong coronal shock. For a source near central meridian the nose of the shock travels towards the Earth, the flux keeps rising as the shock approaches, and the maximum is reached near shock passage. The early intensities are further restrained by the streaming limit (Reames and Ng, 1998), so that the highest fluxes are expected near the shock. This is consistent with Table 2, although we did not identify the shock passages event by event. The flare fluence therefore measures the event in the regime where the maximum is close in time and in connection to the eruption. When the maximum is produced a day or more later by a shock at 1 AU, it depends on the evolution of the shock in the solar wind, which is not contained in observations made at the end of the flare. This also offers a natural reading of the steepening in Figure 1: large eruptions drive shocks that remain strong to 1 AU, and shock-dominated maxima are added to the top of the distribution (median fluence 0.16 against 0.09 J m^{-2}).

We looked for further parameters in the residuals of the fluence law (Table 3). The residual tends to increase with CME speed ($\rho = 0.22$, and $\rho = 0.28$ before 2019, when the catalogued speeds are more homogeneous), in the sense expected for shock acceleration (Kahler, 2001; Gopalswamy et al., 2004; Papaioannou et al., 2024). It tends to decrease with the delay of

the onset, which is not known at the issue time. Neither dependence remains significant after correction for the 17 quantities examined. A previous proton event, which might raise the seed population (Gopalswamy et al., 2004), and the connection factor show no clear residual effect. The flare fluence already absorbs most of what is known at the end of the flare.

5.4. SOLAR CYCLE DIFFERENCES

The median peak flux of the sample falls from 236 pfu in cycle 23 to 73 and 48 pfu in cycles 24 and 25, with the median fluence falling from 0.14 to 0.11 and 0.09 J m^{-2} and the median CME speed from 1674 to 1418 and 1120 km s^{-1} (Table 4). Models trained on all cycles overestimate cycle 24 by about 0.2 dex, which suggests that events of that cycle were weaker than their flares imply. This fits the reduced heliospheric pressure and anomalous CME expansion reported for cycle 24 (Gopalswamy et al., 2014). The published Balch relation performs best on cycle 25 (MAE 0.560 dex). Its calibration on older events has not aged. The change of the GOES flux scale matters little for this result (0.554 dex without rescaling), though the scale should be stated whenever the relation is used or refitted.

5.5. WHAT QUANTUM REGRESSION ADDS

Quantum regression reaches the accuracy of the best classical models, and with few inputs it does so in a particularly economical way (Tables 1, 5, and 6; Figures 3 and 4). With all twelve inputs its MAE is 0.584 dex, a clear improvement on climatology (-0.121 [-0.191, -0.050] dex). With only the fluence and the connection factor it reaches 0.567 dex, with a typical multiplicative error of 3.0 and a correlation of 0.54.

Three properties are worth noting. First, VQR captures the non-linear scaling of Section 5.1 without being told its form. Given the same two inputs, it has a lower error than linear regression (-0.042 [-0.076, -0.011] dex, Wilcoxon $p = 0.01$) and than the refitted power law (-0.036 [-0.070, -0.006] dex, $p = 0.04$), out of sample and with its settings fixed in advance. The parabola of Equation (4), which we selected only after seeing the data, adds nothing further (difference $+0.011$ [-0.033, $+0.054$] dex). The curvature was in fact first indicated by this comparison, so VQR served as a tool for discovery as well as a forecast.

Second, VQR generalizes well. Its training error is close to its forecast error: the gap is 0.01 dex with two inputs and 0.05 dex with twelve, as small as for ridge regression and far below the 0.18 and 0.27 dex of random forests of equal accuracy. With about one hundred events this is a practical merit, because the error seen during training is then a realistic estimate of the error of a forecast.

Third, the two-input model carries over to the newest cycle. On cycle 25 its MAE is 0.567 dex with a bias of $+0.10$ dex, level with the published relation (0.560 dex, bias -0.29 dex) and

below the refitted power law (0.621 dex) and the forest (0.610 dex), although with 26 events these differences are within the uncertainties.

These gains should be seen in proportion. The differences from the published Balch relation, -0.052 [-0.130, $+0.023$] dex for twelve inputs and -0.069 [-0.142, $+0.003$] dex for two, are within the uncertainty, so VQR and the relation are statistically equivalent on these events. More inputs do not help, which agrees with Section 5.3.: the additional observations do not carry the missing information about the shock at 1 AU.

The benefit is also not specifically quantum. The two-input circuit contains no entanglement, and a circuit with repeated encoding computes a truncated Fourier series of its inputs (Schuld, Sweke, and Meyer, 2021). We therefore replaced the circuit by a ridge regression on the sine and cosine of the same quantile-mapped inputs. With the first harmonic alone, which gives four features, the MAE is 0.542 dex, statistically equal to VQR (difference of VQR from it $+0.025$ [-0.012, $+0.064$] dex) and below the published relation (-0.094 [-0.173, -0.019] dex). A classical network with six hidden units and a similar number of weights reaches 0.550 dex. What improves on the power law is thus a smooth non-linear response on a rank-like scale of the fluence, which compact classical models provide equally well.

Entanglement brings no gain here for a physical reason. Entangling two qubits lets the output depend on products of their inputs, that is, on interactions. In these data the fluence and the connection factor act almost independently: adding the interaction term to a linear law changes the MAE from 0.604 to 0.609 dex. Coupling the two qubits accordingly leaves the error unchanged (0.573 dex, difference $+0.006$ [-0.005, $+0.017$] dex). Details of the circuit also matter little for the fluence and connection inputs. One layer does nearly as well as three (Table 7), and revealing the inputs step by step in their physical order, from the pre-flare state to the eruption, gives the same errors (differences of -0.001 [-0.007, $+0.004$] dex with two inputs and -0.007 [-0.024, $+0.009$] dex with twelve). The Garcia inputs are an exception: EM, peak flux, and Δt are strongly correlated with one another, and VQR on these alone has a larger error (0.666 dex) than the staged circuit (0.613 dex) or the refitted Garcia form. Appendix B examines further properties attributed to quantum networks.

5.6. FORECASTS UPDATED AFTER THE ONSET

If the peak flux of many events is set by what happens after the flare, the protons themselves should carry this information once the event has begun. We therefore repeated the forecasts 1, 3, and 6 hours after the NOAA begin time, adding the >10 MeV flux observed at that moment. The flux comes from the hourly OMNI data to 2017 and from GOES-R afterwards, with the gaps filled by the 7.8–25 MeV intensity of SOHO/EPHIN (Müller-Mellin et al., 1995) on a common scale; the EPHIN intensity at the maximum correlates with the NOAA peak flux at 0.91 for 74 events, with a stable offset across the cycles. Only events whose maximum is still

ahead are scored, one year left out.

The improvement is large (Table 8). For the events still rising after 3 hours the MAE falls from 0.62 dex for the fluence law to 0.45 dex for a linear model of fluence and early flux (difference -0.18 [-0.27, -0.09] dex), and after 6 hours from 0.59 to 0.42 dex (difference -0.17 [-0.28, -0.06] dex), that is, from a typical factor of about 4 to about 2.5. For events above 1000 pfu the error at 6 hours falls from 0.80 to 0.58 dex. A small network reaches 0.37 dex at 6 hours and VQR 0.40 dex, and these differences among models are within the uncertainties. VQR has its most favorable result at the earliest time, 0.48 dex after 1 hour, against 0.53 dex for the linear model (difference -0.047 [-0.095, $+0.001$] dex) and the same 0.48 dex for the small network. A forecast of this type also extrapolates naturally, since the observed flux already shows the scale of the event.

6. Discussion

A consistent picture emerges from the Results. The flare fluence acts as a measure of the energy of the eruption, and the relation between this energy and the peak proton flux has held across three solar cycles. The published law of Balch (2008) remains a sound description for a typical event, with a local exponent close to its value of 0.82. The scatter of about a factor of 5 is not random: a large part of it reflects the geometry of the observer relative to the shock. Western, well-connected events reach their maximum early and follow the fluence closely. Events near central meridian reach it at the shock, and their size is set by the later evolution of the shock in the solar wind.

This has a direct consequence for forecasting. At the end of the flare the available observations describe the eruption, not the shock at 1 AU. Any flare-time model, simple or complex, inherits this limit, which is why the classical relation, a random forest, and quantum regression arrive at nearly the same accuracy. Section 5.6. shows that this limit is one of information. A few hours of proton data lower the error by about a third, an effect far larger than any difference among models at the flare end, in the same spirit as the use of the early near-Earth proton flux by the UMASEP model (Núñez, 2011). The trade-off is lead time: the median time from the NOAA begin time to the maximum is short for western events, so the update helps most for events near central meridian, where the maximum lies many hours ahead. Estimates of shock arrival, and a separate treatment of the prompt and shock-dominated components, seem natural next steps.

For users of the relations we offer three remarks. The flux scale must be stated, because the change at GOES-16 corresponds to 0.13 dex in Equation (1). The fitted exponent of a sample selected above a threshold is biased low. And new intensity models should report the skill of Equation (1) on their evaluation events: the formula takes one line of code and is a demanding benchmark.

For quantum models the results suggest a realistic view of their present role in this field. A small variational circuit is a compact and well-behaved way of fitting a smooth non-linear dependence, and here it drew attention to structure that a fixed power law would miss. On this problem, however, compact classical models do the same, so the case for a quantum model has to rest on applications where such equivalence does not hold.

Limitations. The sample is restricted to attributed flares and delays of no more than 24 hours, so events from far behind the limb, which can be seen at the Earth over a wide range of longitudes (Richardson et al., 2014), are underrepresented. Forecasts are conditional on an event, and no false-alarm rate is estimated. The term α is reproduced with an incomplete region match. The emission measures are not on Garcia's calibration. CME speeds after 2019 are inhomogeneous. Shock passages were not identified individually. We did not examine the rise-time formula of Balch (2008) or energies above 10 MeV. The circuits were simulated without noise.

7. Conclusions

1. The peak-flux relation of Balch (2008), with published coefficients, extends to 111 events of cycles 23–25 with its original skill (correlation 0.49, RMSE 0.83 dex), including the first GOES-R cycle, with a mean offset of -0.38 dex.

2. The peak flux depends on the flare fluence in a curved way. The local exponent is 0.85 at $0.1\,\mathrm{J\,m^{-2}}$, in agreement with the published value, and steepens for the largest flares. Accounting for the 10 pfu selection raises the fitted exponent of a single power law from 0.71 to 1.33.

3. The Garcia (2004a) relation orders the events as well as the fluence law but requires a consistent emission-measure calibration. Temperature and emission measure add no information on the peak flux beyond the integrated emission.

4. The scatter is organized by the time of the proton maximum and by longitude. Events that peak within 12 hours (median W58) follow the fluence law, while those peaking after a day (median W11) are underestimated by 0.4–0.7 dex, as expected if their maximum is set near shock passage.

5. Adding the >10 MeV flux observed after the onset lowers the error for events still rising from about 0.6 dex to 0.45 dex after 3 hours and 0.42 dex after 6 hours, an effect much larger than any difference among forecast methods at the flare end.

6. Quantum regression matches the best classical models (MAE 0.567 dex with two inputs, against 0.636 dex for the published law and 0.603 dex for the refitted law). It is statistically equivalent to the published relation on these events and captures the curvature of

the law without an assumed form, with a small generalization gap. Entanglement and additional inputs bring no gain, because the inputs act almost independently and carry no information on the later shock. A ridge regression on four Fourier features (0.542 dex) and a small classical network (0.550 dex) reach the same accuracy, so we find no benefit specific to quantum effects for this problem.

Acknowledgments

The author thanks the NOAA Space Weather Prediction Center and the National Centers for Environmental Information for the proton event list and the GOES XRS data, the NASA/GSFC Space Physics Data Facility for OMNI and CDAWeb, and the ACE, SOHO, and GOES instrument teams. The CME catalogue is generated and maintained at the CDAW Data Center by NASA and the Catholic University of America in cooperation with the Naval Research Laboratory. SOHO is a project of international cooperation between ESA and NASA. The study used the Heliophysics Event Knowledgebase.

Funding

This research did not receive funding.

Data Availability

The data and code that reproduce all numbers, tables, and figures of this article are available at https://github.com/davydenkov/sep-peak-flux-rqnn. The underlying GOES XRS data, the NOAA proton event list, OMNI, ACE EPAM, SOHO/EPHIN, and the CME catalogue are public and are available from NOAA NCEI, NOAA SWPC, NASA CDAWeb, and the CDAW Data Center. The measured X-ray quantities and all forecasts for each event are also given in the Electronic Supplementary Material.

Appendix A. Sensitivity to Input Errors

To learn how sensitive the forecasts are to errors in the observations, we added Gaussian noise with a standard deviation of 10–50 % of that of each input to the validation inputs, with 20 draws per event and the same draws for all models. For the fluence, 50 % corresponds to 0.30 dex, far above the measurement error of GOES. Noise was applied either to all inputs of a model or to the X-ray inputs alone. Two further cases are of operational interest: a missing fluence,

for which the fluence laws use the triangular proxy from the catalogue and other models impute the training median, and X-ray quantities too high by the factor of $1/0.7$ that separates the two GOES scales. We use the increase of the MAE as the measure, because a flat forecast would otherwise appear stable.

Table 9 shows that noise of this size matters little for any model, since it is small compared with the intrinsic scatter of about 0.7 dex. At 50 % noise on all inputs the MAE rises by 0.026 dex for the twelve-qubit circuit and 0.031 dex for Equation (1), a paired difference of -0.006 [-0.025, $+0.014$] dex. Ridge regression changes least (0.007 dex) because its forecasts are the flattest, and the parabola most (0.052 dex) because curvature amplifies input errors, though its error remains among the lowest. With a missing fluence the proxy keeps the fluence laws near their usual scores. With the wrong flux scale the published law improves slightly because its offset is negative, and the refitted models lose 0.01–0.03 dex.

Entanglement does not change this picture. At 30 % noise the forecasts of the full circuit move by a similar amount to those of a circuit without entangling gates (difference $+0.000$ [-0.005, $+0.006$] dex), and the same holds at 50 % (-0.005 [-0.013, $+0.003$] dex). These intervals are not corrected for the many comparisons involved.

Appendix B. Properties Attributed to Quantum Networks

Several properties are often attributed to quantum neural networks, such as high expressive power with few parameters (Abbas et al., 2021), and comparisons with simple classical models have been recommended (Bowles, Ahmed, and Schuld, 2024). We measured those that can be examined with these data (Table 10), with the two-input circuit unless stated.

Extrapolation. Trained on the events below 1000 pfu, VQR forecasts at most 269 pfu for the 18 larger events, below the training maximum of 956 pfu, and none of its forecasts exceeds that maximum. This is structural: the quantile mapping saturates beyond the training range and the expectation values are bounded. A physical law does extrapolate. A power law fitted with the truncation of the sample taken into account has an MAE of 1.04 dex for these events, against 1.44 dex for VQR and 1.35 dex for Equation (1), and 56 % of its forecasts exceed the training maximum. Adding a circuit or a small classical network to correct its residual does not improve on it (1.27 and 1.27 dex). Among these 18 events the correlation of the peak flux with the fluence is only 0.20, so the size of an unprecedented event is not contained in the flare fluence. For events in the top quarter of the fluence, with training on the rest, the bounded response of VQR keeps its error below that of a power law, but tree models do the same.

Small samples. With about 20 training events and two inputs the network does better than ridge regression and a random forest and is close to the fluence law and a small classical network. With six inputs the forest does as well.

Smoothness. The response to the fluence, measured by the summed absolute second difference along a grid of 200 points, is much smoother than that of a random forest and less smooth than those of a small network or a parabola. This smoothing is a property of a low-order Fourier series and not of a quantum state.

Trainability. The variance of the gradient of the circuit output falls by a factor of only 1.2 per qubit between 2 and 12 qubits, with no sign of a barren plateau (McClean et al., 2018). The behavior is similar for random parameters and reflects the small depth of the circuit.

Cost. Training a twelve-qubit circuit takes about 153 seconds on a classical computer, against 0.2 seconds for a random forest. No statement on speed can be made for quantum hardware, which we did not use.

These results concern noiseless simulations of up to twelve qubits and about one hundred events, and they do not exclude benefits on other problems.

References

Abbas, A., Sutter, D., Zoufal, C., Lucchi, A., Figalli, A., Woerner, S.: 2021, Nature Comput. Sci. **1**, 403. DOI: 10.1038/s43588-021-00084-1

Alberti, T., Laurenza, M., Cliver, E.W., Storini, M., Consolini, G., Lepreti, F.: 2017, Astrophys. J. **838**, 59. DOI: 10.3847/1538-4357/aa5cb8

Ali, A., Sadykov, V., Kosovichev, A., Kitiashvili, I.N., Oria, V., Nita, G.M., et al.: 2024, Astrophys. J. Suppl. **270**, 15. DOI: 10.3847/1538-4365/ad0a6c

Ali, M.A., Abdelkawy, A.G.A., Shaltout, A.M.K., Beheary, M.M.: 2025, Sci. Rep. **15**, 9546. DOI: 10.1038/s41598-025-92207-1

Anastasiadis, A., Papaioannou, A., Sandberg, I., Georgoulis, M., Tziotziou, K., Kouloumvakos, A., et al.: 2017, Solar Phys. **292**, 134. DOI: 10.1007/s11207-017-1163-7

Bain, H.M., Steenburgh, R.A., Onsager, T.G., Stitely, E.M.: 2021, Space Weather **19**, e2020SW002670. DOI: 10.1029/2020SW002670

Balch, C.C.: 1999, Radiat. Meas. **30**, 231. DOI: 10.1016/S1350-4487(99)00052-9

Balch, C.C.: 2008, Space Weather **6**, S01001. DOI: 10.1029/2007SW000337

Belov, A.: 2009, Adv. Space Res. **43**, 467. DOI: 10.1016/j.asr.2008.08.011

Belov, A., Garcia, H., Kurt, V., Mavromichalaki, H., Gerontidou, M.: 2005, Solar Phys. **229**, 135. DOI: 10.1007/s11207-005-4721-3

Bowles, J., Ahmed, S., Schuld, M.: 2024, preprint. arXiv:2403.07059

Breiman, L.: 2001, Mach. Learn. **45**, 5. DOI: 10.1023/A:1010933404324

Cane, H.V., Reames, D.V., von Rosenvinge, T.T.: 1988, J. Geophys. Res. **93**, 9555. DOI: 10.1029/JA093iA09p09555

Cliver, E.W., Kahler, S.W., Reames, D.V.: 2004, Astrophys. J. **605**, 902. DOI: 10.1086/382651

Desai, M., and Giacalone, J.: 2016, Living Rev. Solar Phys. **13**, 3. DOI: 10.1007/s41116-016-0002-5

Dierckxsens, M., Tziotziou, K., Dalla, S., Patsou, I., Marsh, M.S., Crosby, N.B., et al.: 2015, Solar Phys. **290**, 841. DOI: 10.1007/s11207-014-0641-4

Efron, B., and Tibshirani, R.J.: 1993, An Introduction to the Bootstrap, Chapman and Hall, New York. DOI: 10.1201/9780429246593

Emslie, A.G., Dennis, B.R., Shih, A.Y., Chamberlin, P.C., Mewaldt, R.A., Moore, C.S., et al.: 2012,

Astrophys. J. **759**, 71. DOI: 10.1088/0004-637X/759/1/71

Garcia, H.A.: 1994a, Solar Phys. **154**, 275. DOI: 10.1007/BF00681100

Garcia, H.A.: 1994b, Astrophys. J. **420**, 422. DOI: 10.1086/173572

Garcia, H.A.: 2004a, Space Weather **2**, S02002. DOI: 10.1029/2003SW000001

Garcia, H.A.: 2004b, Space Weather **2**, S06003. DOI: 10.1029/2003SW000035

Gold, R.E., Krimigis, S.M., Hawkins, S.E., Haggerty, D.K., Lohr, D.A., Fiore, E., et al.: 1998, Space Sci. Rev. **86**, 541. DOI: 10.1023/A:1005088115759

Gopalswamy, N., Yashiro, S., Krucker, S., Stenborg, G., Howard, R.A.: 2004, J. Geophys. Res. **109**, A12105. DOI: 10.1029/2004JA010602

Gopalswamy, N., Yashiro, S., Michalek, G., Stenborg, G., Vourlidas, A., Freeland, S., et al.: 2009, Earth Moon Planets **104**, 295. DOI: 10.1007/s11038-008-9282-7

Gopalswamy, N., Akiyama, S., Yashiro, S., Xie, H., Mäkelä, P., Michalek, G.: 2014, Geophys. Res. Lett. **41**, 2673. DOI: 10.1002/2014GL059858

Hosseinzadeh, P., Filali Boubrahimi, S., Hamdi, S.M.: 2024, Space Weather **22**, e2024SW003982. DOI: 10.1029/2024SW003982

Hurlburt, N., Cheung, M., Schrijver, C., Chang, L., Freeland, S., Green, S., et al.: 2012, Solar Phys. **275**, 67. DOI: 10.1007/s11207-010-9624-2

Janssens, J., Delouille, V., Clette, F., Andries, J.: 2025, J. Space Weather Space Clim. **15**, 14. DOI: 10.1051/swsc/2025007

Kahler, S.W.: 1982, J. Geophys. Res. **87**, 3439. DOI: 10.1029/JA087iA05p03439

Kahler, S.W.: 2001, J. Geophys. Res. **106**, 20947. DOI: 10.1029/2000JA002231

Kahler, S.W., and Ling, A.G.: 2018, J. Space Weather Space Clim. **8**, A47. DOI: 10.1051/swsc/2018033

Kahler, S.W., and Ling, A.G.: 2020, Astrophys. J. **901**, 63. DOI: 10.3847/1538-4357/abae5e

Kahler, S.W., and Ling, A.G.: 2022, Astrophys. J. **934**, 175. DOI: 10.3847/1538-4357/ac7e56

Kahler, S.W., and Ling, A.G.: 2023, Astrophys. J. **956**, 24. DOI: 10.3847/1538-4357/acf1ff

Kahler, S.W., Cliver, E.W., Ling, A.G.: 2007, J. Atmos. Solar-Terr. Phys. **69**, 43. DOI: 10.1016/j.jastp.2006.06.009

Kasapis, S., Zhao, L., Chen, Y., Wang, X., Bobra, M., Gombosi, T.: 2022, Space Weather **20**, e2021SW002842. DOI: 10.1029/2021SW002842

King, J.H., and Papitashvili, N.E.: 2005, J. Geophys. Res. **110**, A02104. DOI: 10.1029/2004JA010649

Laurenza, M., Cliver, E.W., Hewitt, J., Storini, M., Ling, A.G., Balch, C.C., et al.: 2009, Space Weather **7**, S04008. DOI: 10.1029/2007SW000379

Lavasa, E., Giannopoulos, G., Papaioannou, A., Anastasiadis, A., Daglis, I.A., Aran, A., et al.: 2021, Solar Phys. **296**, 107. DOI: 10.1007/s11207-021-01837-x

McClean, J.R., Boixo, S., Smelyanskiy, V.N., Babbush, R., Neven, H.: 2018, Nature Commun. **9**, 4812. DOI: 10.1038/s41467-018-07090-4

Müller-Mellin, R., Kunow, H., Fleißner, V., Pehlke, E., Rode, E., Röschmann, N., et al.: 1995, Solar Phys. **162**, 483. DOI: 10.1007/BF00733437

Núñez, M.: 2011, Space Weather **9**, S07003. DOI: 10.1029/2010SW000640

Papaioannou, A., Vainio, R., Raukunen, O., Jiggens, P., Aran, A., Dierckxsens, M., et al.: 2022, J. Space Weather Space Clim. **12**, 24. DOI: 10.1051/swsc/2022019

Papaioannou, A., Herbst, K., Ramm, T., Cliver, E.W., Lario, D., Veronig, A.M.: 2023, Astron. Astrophys. **671**, A66. DOI: 10.1051/0004-6361/202243407

Papaioannou, A., Herbst, K., Ramm, T., Lario, D., Veronig, A.M.: 2024, Astron. Astrophys. **690**, A60. DOI: 10.1051/0004-6361/202450705

Papaioannou, A., Strauss, R.D., Lario, D., Vainio, R., Wijsen, N., Afanasiev, A., et al.: 2025, Space Sci. Rev. **221**, 82. DOI: 10.1007/s11214-025-01211-4

Pérez-Salinas, A., Cervera-Lierta, A., Gil-Fuster, E., Latorre, J.I.: 2020, Quantum **4**, 226. DOI: 10.22331/q-2020-02-06-226

Reames, D.V.: 1999, Space Sci. Rev. **90**, 413. DOI: 10.1023/A:1005105831781

Reames, D.V.: 2013, Space Sci. Rev. **175**, 53. DOI: 10.1007/s11214-013-9958-9

Reames, D.V., and Ng, C.K.: 1998, Astrophys. J. **504**, 1002. DOI: 10.1086/306124

Richardson, I.G., von Rosenvinge, T.T., Cane, H.V., Christian, E.R., Cohen, C.M.S., Labrador, A.W., et al.: 2014, Solar Phys. **289**, 3059. DOI: 10.1007/s11207-014-0524-8

Rotti, S.A., Aydin, B., Martens, P.C.: 2024, Astrophys. J. **966**, 165. DOI: 10.3847/1538-4357/ad374e

Ryan, D.F., Milligan, R.O., Gallagher, P.T., Dennis, B.R., Tolbert, A.K., Schwartz, R.A., et al.: 2012, Astrophys. J. Suppl. **202**, 11. DOI: 10.1088/0067-0049/202/2/11

Schuld, M., Sweke, R., Meyer, J.J.: 2021, Phys. Rev. A **103**, 032430. DOI: 10.1103/PhysRevA.103.032430

Struminsky, A.B., Sadovskii, A.M., Grigorieva, I.Yu.: 2024, Geomagn. Aeron. **64**, 139. DOI: 10.1134/S0016793223600984

Swalwell, B., Dalla, S., Walsh, R.W.: 2017, Solar Phys. **292**, 173. DOI: 10.1007/s11207-017-1196-y

Thomas, R.J., Starr, R., Crannell, C.J.: 1985, Solar Phys. **95**, 323. DOI: 10.1007/BF00152409

Trottet, G., Samwel, S., Klein, K.-L., Dudok de Wit, T., Miteva, R.: 2015, Solar Phys. **290**, 819. DOI: 10.1007/s11207-014-0628-1

White, S.M., and Desnoes, D.: 2026, Solar Phys. **301**, 28. DOI: 10.1007/s11207-026-02618-0

White, S.M., Thomas, R.J., Schwartz, R.A.: 2005, Solar Phys. **227**, 231. DOI: 10.1007/s11207-005-2445-z

Whitman, K., Egeland, R., Richardson, I.G., Allison, C., Quinn, P., Barzilla, J., et al.: 2023, Adv. Space Res. **72**, 5161. DOI: 10.1016/j.asr.2022.08.006

Wilcoxon, F.: 1945, Biometrics Bull. **1**, 80. DOI: 10.2307/3001968

Yashiro, S., Gopalswamy, N., Michalek, G., St. Cyr, O.C., Plunkett, S.P., Rich, N.B., et al.: 2004, J. Geophys. Res. **109**, A07105. DOI: 10.1029/2003JA010282

Yu, Y., Chen, Y., Zhao, L., Whitman, K., Manchester, W., Gombosi, T.: 2026, Sci. Rep., in press. DOI: 10.1038/s41598-026-66110-2

Figure Legends

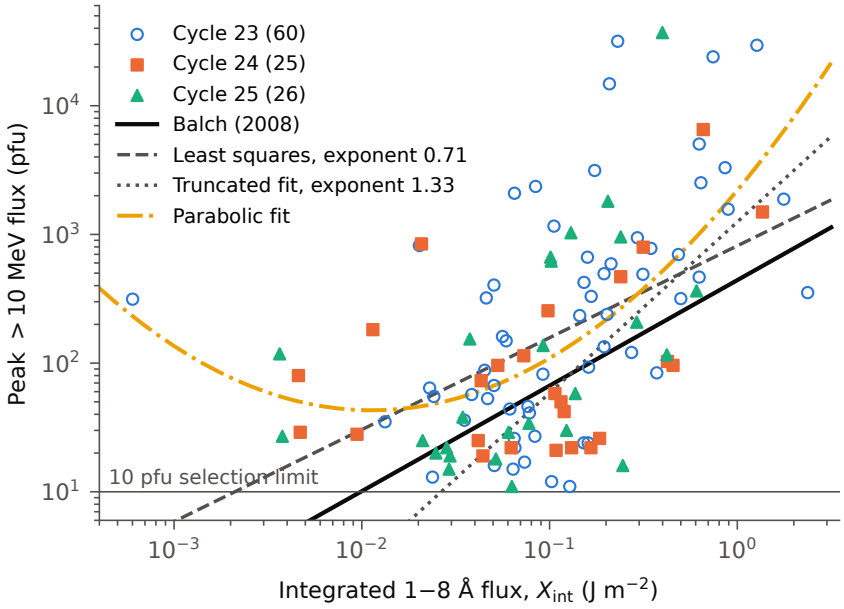


Figure 1: Peak >10 MeV proton flux against the 1–8 Å flux integrated from flare onset to the half-power point, on the operational GOES scale. Symbols mark solar cycles 23 (open circles), 24 (squares), and 25 (triangles); the numbers of events are in the key. The solid line is Equation (1) with $\alpha = 1$, the dashed line a least-squares fit, the dotted line a fit that allows for the truncation of the sample at 10 pfu (thin horizontal line), and the dash-dotted line the parabolic fit of Equation (4).

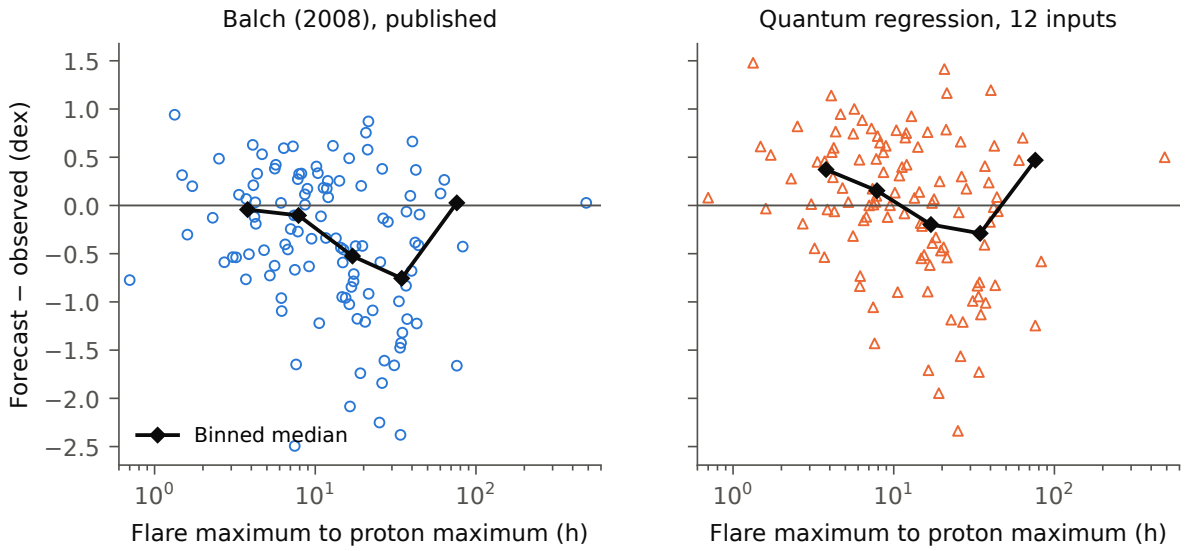


Figure 2: Forecast error against the time from the flare maximum to the proton maximum for the published Balch relation (left) and quantum regression with twelve inputs (right). Diamonds connect medians in the bins 0–6, 6–12, 12–24, 24–48, and more than 48 hours. The time of maximum is not known at the issue time and is used here only as a diagnostic.

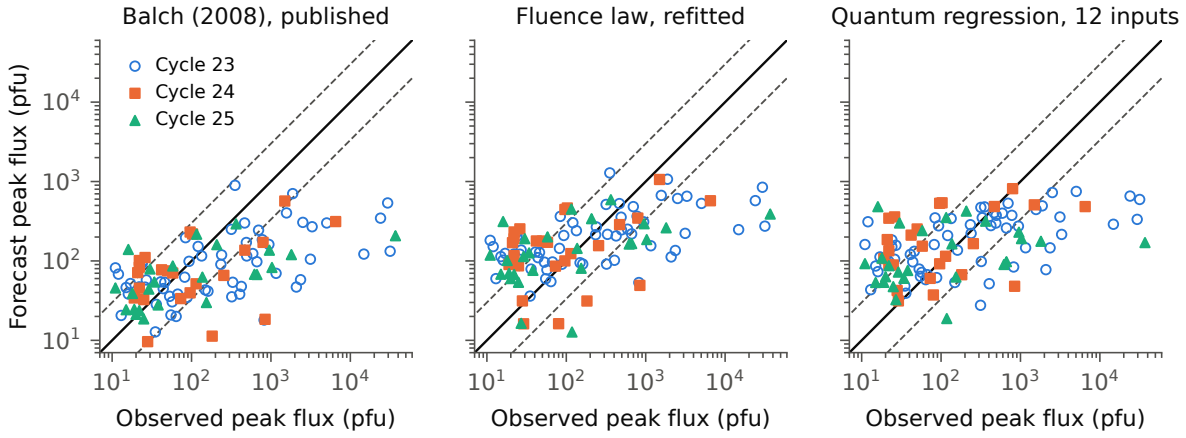


Figure 3: Forecast against observed peak flux for the published Balch relation, the refitted fluence law, and quantum regression with twelve inputs. The refitted law and quantum regression are out-of-sample forecasts with one year left out. Solid lines mark equality, dashed lines a factor of 3.

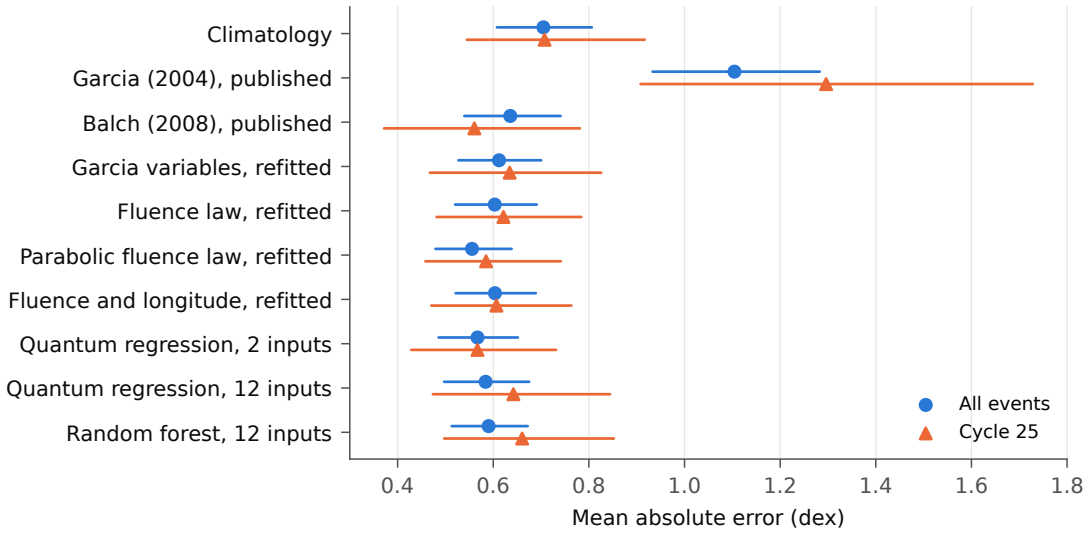


Figure 4: Mean absolute error of the logarithm of the peak flux with 95 % bootstrap intervals, for all 111 events (circles) and the 26 events of cycle 25 (triangles).

Tables

Table 1: Forecast scores of the peak >10 MeV flux for 111 proton events. MAE is the mean absolute error of the logarithm with the 95 % bootstrap interval, $\times$ the median multiplicative error, $\leq \times 3$ the percentage of forecasts within a factor of 3, and r the Pearson correlation of the logarithms.

Model	MAE [dex]	Bias	RMSE	$\times$	$\leq \times 3$	r
No flare information						
Climatology (training median)	0.705 [0.61, 0.81]	−0.19	0.88	4.3	35	⋯
Published, no fitting to this sample						
Balch (2008), published	0.636 [0.54, 0.74]	−0.38	0.83	2.9	50	0.49
Garcia (2004), published	1.104 [0.93, 1.28]	−1.04	1.44	7.4	29	0.45
Refitted, leave one year out						
Fluence law, refitted	0.603 [0.52, 0.69]	−0.01	0.75	3.6	42	0.46
Parabolic fluence law, refitted	0.556 [0.48, 0.64]	+0.00	0.70	2.8	53	0.58
Fluence and longitude, refitted	0.604 [0.52, 0.69]	−0.01	0.75	3.4	46	0.47
Garcia variables, refitted	0.612 [0.53, 0.70]	−0.00	0.76	3.3	47	0.44
Non-linear and multi-input models, leave one year out						
Quantum regression, 2 inputs	0.567 [0.49, 0.65]	−0.01	0.71	3.0	50	0.54
Quantum regression, 6 inputs	0.572 [0.49, 0.66]	−0.01	0.72	3.0	50	0.53
Quantum regression, 12 inputs	0.584 [0.50, 0.68]	−0.01	0.75	3.3	47	0.48
Random forest, 12 inputs	0.590 [0.51, 0.67]	+0.00	0.73	3.1	48	0.52
Ridge regression, 12 inputs	0.624 [0.54, 0.71]	−0.01	0.78	3.8	41	0.41

Table 2: Proton events by the time from the flare maximum to the proton maximum: number of events, median flare longitude, percentage of eastern sources, median X_{int} ($\mathrm{J\,m^{-2}}$), median CME speed ($\mathrm{km\,s^{-1}}$), median peak flux (pfu), number of events above 1000 pfu, and mean forecast error in dex of the published Balch relation and of VQR with twelve inputs.

Maximum	N	Lon.	East	X_{int}	V_{CME}	Peak	>1000	Balch	VQR
Within 12 h	56	W58	7	0.09	1450	61	3	-0.16	0.23
12–24 h	26	W48	12	0.10	1556	168	6	-0.47	-0.13
After 24 h	29	W11	34	0.16	1557	364	9	-0.72	-0.36

Table 3: Spearman correlation of the out-of-sample residual of the refitted fluence law with physical quantities, with 95 % bootstrap intervals, p values, and Holm-adjusted p values over the 17 quantities. The delay is not known at the issue time and is included as a diagnostic.

Quantity	N	ρ	p	p_{Holm}
Delay	111	-0.24 [-0.41, -0.06]	0.013	0.22
CME speed (pre-2019)	68	$+0.28$ [$+0.06$, $+0.48$]	0.021	0.34
CME speed	82	$+0.22$ [$+0.01$, $+0.41$]	0.043	0.64
West longitude	111	-0.18 [-0.36, $+0.01$]	0.055	0.76
CME width	82	$+0.21$ [-0.01, $+0.43$]	0.055	0.76
Type III power	106	$+0.14$ [-0.07, $+0.33$]	0.151	1.00
Microwave 2.7 GHz	87	$+0.14$ [-0.07, $+0.33$]	0.195	1.00
Background J10	66	$+0.15$ [-0.09, $+0.37$]	0.223	1.00
Prior SEP 72 h	111	-0.10 [-0.29, $+0.10$]	0.284	1.00
Connection factor	111	-0.10 [-0.28, $+0.10$]	0.311	1.00
Peak 1-8 A flux	111	$+0.07$ [-0.11, $+0.25$]	0.469	1.00
T (GOES)	111	-0.06 [-0.25, $+0.15$]	0.538	1.00
Early proton rise	101	$+0.06$ [-0.15, $+0.25$]	0.571	1.00
Near-rel. electrons	110	$+0.02$ [-0.17, $+0.22$]	0.799	1.00
Absolute latitude	111	$+0.02$ [-0.17, $+0.19$]	0.839	1.00
Rise time	111	$+0.01$ [-0.19, $+0.21$]	0.938	1.00
Duration (25 %)	111	-0.00 [-0.20, $+0.19$]	0.978	1.00

Table 4: Mean absolute error and, in parentheses, bias in dex by solar cycle with one year left out, and for models trained on events before 2020 and applied to cycle 25 (holdout). Numbers of events are in parentheses in the heading.

Model	Cycle 23 (60)	Cycle 24 (25)	Cycle 25 (26)	Holdout (26)
Climatology (training median)	0.77 (−0.38)	0.54 (+0.04)	0.71 (+0.00)	0.68 (+0.03)
Balch (2008), published	0.70 (−0.48)	0.57 (−0.22)	0.56 (−0.29)	0.56 (−0.29)
Garcia (2004), published	1.07 (−1.03)	0.98 (−0.87)	1.30 (−1.22)	1.30 (−1.22)
Fluence law, refitted	0.62 (−0.13)	0.56 (+0.16)	0.62 (+0.10)	0.62 (+0.13)
Parabolic fluence law, refitted	0.56 (−0.09)	0.51 (+0.17)	0.58 (+0.07)	0.59 (+0.10)
Garcia variables, refitted	0.63 (−0.10)	0.55 (+0.20)	0.63 (+0.04)	0.62 (+0.06)
Quantum regression, 12 inputs	0.58 (−0.14)	0.54 (+0.22)	0.64 (+0.06)	0.60 (+0.05)
Random forest, 12 inputs	0.58 (−0.14)	0.55 (+0.26)	0.66 (+0.10)	0.66 (+0.08)

Table 5: Paired differences of the mean absolute error in dex, with 95 % bootstrap intervals, for 111 events. A negative value means that the first model has the lower error.

First model	Second model	Difference
VQR, 12 inputs	Climatology	−0.121 [−0.191, −0.050]
VQR, 12 inputs	Balch (2008), published	−0.052 [−0.130, +0.023]
VQR, 12 inputs	Fluence law, refitted	−0.019 [−0.057, +0.017]
VQR, 12 inputs	Random forest, 12 inputs	−0.006 [−0.049, +0.037]
VQR, 2 inputs	Balch (2008), published	−0.069 [−0.142, +0.003]
VQR, 2 inputs	Fluence law, refitted	−0.036 [−0.070, −0.006]
VQR, 2 inputs	Ridge regression, 2 inputs	−0.042 [−0.076, −0.011]
VQR, 2 inputs	Random forest, 2 inputs	−0.007 [−0.058, +0.046]
VQR, 2 inputs	Parabolic fluence law	+0.011 [−0.033, +0.054]
Parabolic fluence law	Balch (2008), published	−0.080 [−0.159, −0.005]
Parabolic fluence law	Fluence law, refitted	−0.047 [−0.103, +0.002]
Fluence law, refitted	Climatology	−0.102 [−0.177, −0.026]

Table 6: Mean absolute error in dex with the same inputs in each row, for VQR, ridge regression, and a random forest, with one year left out. The last column gives the VQR error for the 26 events of cycle 25. The published and refitted relations are in Table 1.

Inputs	Qubits	VQR	Ridge	Forest	VQR, cycle 25
Fluence, connection	2	0.567	0.609	0.574	0.567
Emission measure, peak flux, duration	3	0.666	0.607	0.603	0.686
All five X-ray and connection inputs	5	0.588	0.610	0.594	0.582
Six flare inputs, measured fluence	6	0.572	0.622	0.602	0.599
Twelve inputs, measured fluence	12	0.584	0.624	0.590	0.642

Table 7: Mean absolute error in dex of circuit variants on the same inputs: inputs revealed in stages in their physical order (staged), the VQR used in this article with three layers, one layer, and a random forest. The last two columns give the number of circuit parameters.

Inputs	Staged	Three layers	One layer	Forest	Par. (1)	Par. (3)
Fluence, connection	0.568	0.567	0.587	0.574	8	24
Six flare inputs	0.567	0.572	0.581	0.602	28	84
Twelve inputs	0.591	0.584	0.582	0.590	60	180

Table 8: Mean absolute error in dex of forecasts issued 1, 3, and 6 hours after the NOAA begin time, for events whose maximum is still ahead. The last column gives the error at 6 hours for events above 1000 pfu. The fluence law and the Balch relation use no proton data.

Model	1 h	3 h	6 h	6 h, >1000 pfu
Events	83	70	56	12
Balch (2008), published	0.63	0.67	0.68	1.27
Fluence law, refitted	0.59	0.62	0.59	0.80
Early flux, linear	0.53	0.45	0.42	0.64
Fluence and early flux, linear	0.53	0.45	0.42	0.58
With connection, linear	0.52	0.44	0.40	0.52
Random forest	0.48	0.43	0.41	0.69
Small network	0.48	0.44	0.37	0.52
VQR, 3 inputs	0.48	0.44	0.40	0.53

Table 9: Robustness to input errors. Mean absolute error in dex on clean data; its increase with Gaussian noise of 30 % and 50 % of the standard deviation of all inputs, and of the X-ray inputs only; and its value with a missing fluence and with all X-ray quantities too high by a factor of $1/0.7$. Measured fluence is used. Noise is averaged over 20 draws per event.

Model	Clean	All, 30 %	All, 50 %	X-ray, 50 %	Missing	Scale
Balch (2008), published	0.636	0.011	0.031	0.031	0.657	0.608
Fluence law, refitted	0.603	0.010	0.026	0.026	0.608	0.620
Parabolic fluence law	0.556	0.018	0.052	0.052	0.562	0.579
Garcia variables, refitted	0.624	0.010	0.029	0.029	0.624	0.647
Ridge regression, 12 inputs	0.624	0.003	0.007	0.005	0.659	0.636
Random forest, 12 inputs	0.590	0.007	0.026	0.025	0.658	0.603
Quantum regression, 2 inputs	0.567	0.020	0.042	0.042	0.699	0.600
Quantum regression, 6 inputs	0.572	0.015	0.031	0.030	0.671	0.600
Quantum regression, 12 inputs	0.584	0.011	0.026	0.024	0.645	0.615
Quantum regression, no entanglement	0.590	0.017	0.034	0.021	0.645	0.620

Table 10: Measured properties of VQR with fluence and connection as inputs, and of classical references. Errors are mean absolute errors in dex. Roughness is defined in Appendix B. Small-sample and gap values are means over ten random divisions by year.

Property	VQR	Classical references
Error, one year left out	0.567	Ridge 0.609, small network 0.550, Fourier 0.542, forest 0.574
Events $\geq$1000 pfu, trained below	1.44	Balch 1.35, parabola 1.29, forest 1.45
Highest such forecast (pfu)	269	Balch 704, parabola 1211
Top quarter of fluence, trained below	0.62	Balch 0.69, power law 0.75, forest 0.64
About 20 training events	0.597	Power law 0.613, ridge 0.640, forest 0.639, small network 0.609
Gap, about 80 training events	0.008	Ridge 0.015, forest 0.163, small network 0.005
Roughness of the response	0.22	Forest 5.54, small network 0.02, parabola 0.03

Supplementary Files

This is a list of supplementary files associated with this preprint. Click to download.

- esmevents.csv